Finite element modelling strategy for determining directivity of thermoelastically generated laser ultrasound

Xin L. Tu [a],[*], Jie Zhang [a], Alberto M. Gambaruto [b], Paul D. Wilcox [a]

[a] *School of Electrical, Electronic and Mechanical Engineering, University of Bristol, Queen's Building, Bristol, BS8 1TR, UK*
[b] *School of Engineering Mathematics and Technology, Ada Lovelace Building, Bristol, BS8 1TW, UK*

ARTICLE INFO

ABSTRACT

Laser ultrasound (LU) is a contactless and couplant-free remote non-destructive (NDE) technique, which uses lasers for ultrasonic generation and detection rather than conventional piezoelectric transducers. For a transducer, an important characteristic is the directivity, the angle-dependent amplitude of the ultrasonic waves generated in the material. In the non-destructive thermoelastic regime, LU source has been widely modelled as a surface force dipole. However, the directivity of LU in more complex material, where there is an increasing demand for NDE, such as carbon fibre reinforced plastic (CFRP), is yet to be understood. In the current paper, a finite element (FE) modelling methodology to obtain the directivity of LU in complex material is presented. The method is applied to a conductive isotropic material (aluminium, Al) for validation against an existing analytical solution and then applied to a heterogeneous anisotropic material (carbon-fibre reinforced plastic, CFRP). To get the directivity of a specific wave mode, the signal for that mode needs to be resolved in time from other modes at all angles. This is challenging for shear (S) waves in a small model domain due to the head wave, so a technique for suppressing the head wave is shown. The multi-physics model solves for thermal expansion, which models the laser source as a surface heat flux for the Al case, and a buried heat source for the CFRP case, according to where the energy is deposited in the material. The same ultrasound generation pattern can be obtained by using a suitable pure elastodynamic loading, which is shown to be a surface force dipole as per the validation case for Al, and a buried quadrupole for the CFRP case. The modelled directivities are scaled and fitted to experimental measurements using maximum likelihood, and the goodness of fit is discussed. For the Al case, the S wave is preferred over the longitudinal (L) wave for inspection due to greater signal amplitude. For the CFRP case, the quasi-longitudinal (qL) wave in CFRP shows a maximum amplitude directly below the source, and has a greater amplitude than the quasi-shear (qS) wave, suggesting a better choice for inspection.

1. Introduction

The ability to generate and detect ultrasonic waves by lasers extends the application of non-destructive evaluation (NDE) by ultrasonic waves to hazardous environments and complex geometries, because of the contact- and couplant-free nature of the technique, and the small footprint on the inspection face [1,2]. It also offers flexible phased array layouts which can be achieved by optical scanning [3,4]. Therefore, laser ultrasound (LU) is gaining importance in the nuclear, aerospace, and additive manufacturing industry for quality control and in-service inspection [5–7].

By strict definition of NDE, LU must be performed in the thermoelastic regime, which is the focus of the present work. In this scenario, the laser power is kept below the damage threshold of the material. The ultrasonic waves are generated by rapid thermal expansion of a localised region of the material as a result of laser heating. In the ablation regime, the laser power is stronger such that the superficial layer of the material is vapourised, exerting a force normal to the surface in the process. This mechanism is applicable to scenarios where signal strength is prioritised over surface quality, such as in-line grain size monitoring for hot rolling [8,9].

For a transduction method like LU, it is important to know the angle-dependent amplitude of the bulk waves generated, which is known as the directivity. The directivity is useful in the design of inspections, for example to maximise signal strength or to reduce scan time. While the directivity of LU in isotropic metallic material has been studied and a surface dipole model of the laser source has been widely accepted [3,10], there is still a lack of understanding of the LU

---

* Corresponding author.
  E-mail address: xt16846@bristol.ac.uk (X.L. Tu).

directivity in other common engineering materials, such as composites. In those cases, the surface dipole model is potentially invalid due to more complicated interaction between the laser and the material, which comes from material heterogeneity and anisotropy. This leads to the use of different models for the laser source, for example, a buried source for carbon fibre reinforced plastic (CFRP) [11]. In this case, the resin layer covering the outermost fibres is assumed to be transparent to the generation laser, and hence the heat energy is absorbed on the outermost fibre-resin interface. There is also no closed form solution for computing directivity in anisotropic media.

Therefore, this paper aims to provide a general strategy for determining the directivity of laser generated ultrasonic waves in different materials using FE. The FE models can range from full multi-physics simulations that potentially include everything from optical absorption, optical to thermal energy conversion, thermal expansion and elastodynamic wave simulation, to pure elastodynamic models where the laser source is modelled by a suitable multipole force. First, an example use case of applying the FE strategy to different source types is demonstrated in an isotropic, homogeneous material (aluminium, Al). The LU source is first represented by a surface heat flux in a multi-physics model solving for thermal expansion, and second as a surface force dipole in a pure elastodynamic model. The latter is used to provide a benchmark result that can be compared to the analytical solution. Then the modelling strategy is extended to multi-physics simulations of thermoelastically generated ultrasound in heterogeneous anisotropic half spaces, by investigating the LU directivity in CFRP. The rest of the paper is organised as follows. Section 2 details the FE modelling approach and Section 3 the experimental process of measuring the directivity. Section 4 shows the modelled directivities of different scenarios, and discusses the effect of the source types by comparing to the experimental data for Al and CFRP. Section 5 summarises the key findings.

2. FE modelling method

The general strategy to obtain the LU directivity from FE models consists of the following steps:

1. Set up the FE model. This includes the general simulation domain specifications and model-specific excitation methods.
2. Apply the head wave suppression process to the FE model results, to separate the shear wave from the head wave.
3. Separate the bulk wave modes and extract the directivity from the FE results.

The following sections provide the details for each step.

2.1. FE model specification

2D models [12] are simulated, with a symmetry boundary condition applied along the centreline of the domain at the LU source location to reduce the computation burden. The model has a 10×10 mm domain as a trade off between the computational cost and the distance needed to allow different wave modes to separate in the time domain. The top surface is stress-free. Absorbing layers with width of 1 mm were applied around the simulation domain [13]. In addition, low-reflecting boundaries were applied to the outer boundary of the absorbing layers to suppress wave reflections. The laser source was modelled as a heat flux, Q, into the material, and the temperature, T, of the material was governed by

$$\rho C_p \left(\frac{\partial T}{\partial t} \right) + \nabla \cdot \mathbf{q} = Q,$$

where ρ is the density of the material, C_p is the specific heat capacity under constant pressure, $\mathbf{q} = -\mathbf{k} \nabla T$ is heat transfer by conduction within the material, and $\mathbf{k}$ is the thermal conductivity of the material

as a diagonal tensor. The local increase in temperature, ΔT, induces thermal strain, ϵ_{th},

$$\epsilon_{th} = \alpha \Delta T$$

where α is the thermal expansion coefficient of the material. ϵ_{th} from thermal expansion provides a multi-physics coupling to the equation of motion,

$$\rho \frac{\partial^2 \mathbf{u}}{\partial t^2} = \nabla \cdot \sigma + \mathbf{F},$$

where $\mathbf{u}$ is the displacement vector, and $\mathbf{F}$ represents externally-applied force. The material is modelled to have linear elasticity, so the stress tensor $\sigma = C : \epsilon$, is obtained by the Hooke's law, where C is the material stiffness matrix and ϵ the strain tensor including both the strain due to deformation and temperature change, $\epsilon = \epsilon_{mech} + \epsilon_{th}$ [12]. In the multi-physics model, there is no externally applied force, $\mathbf{F} = 0$, and the excitation of waves is solely due to thermal strain, ϵ_{th}, generated by the heat source; in the elastodynamic model, the heat source is represented by an equivalent externally-applied force via $\mathbf{F}$. Schematic drawings of the simulation domains are shown in Fig. 1, and the models employing different excitation methods are introduced in the following sections.

The mesh consists of linear triangular elements. The mesh element size was specified to be 30 elements per shear wavelength [13] at 10 MHz to allow sufficient resolution to the wave motion when the target centre frequency is 5 MHz. The time step was set to 5 ns to fulfil a stable CFL condition.

2.1.1. Surface source in isotropic half space

A surface heat flux shown in Fig. 1a can well approximate the thermoelastic LU source for most metallic components, due to the low penetration depth of the laser compared to the ultrasonic wavelengths of interest in NDE. To simulate a pulsed laser line source, the applied surface heat flux has a Gaussian profile in both space and time, defined by

$$Q(x,t) = e^{-\left(\frac{x}{r_{spot}}\right)^2} e^{-\frac{(t-2\tau_p)^2}{(\tau_p/2)^2}}, \tag{1}$$

where r_{spot} is the full width at half maximum (FWHM) of 0.2 mm, and τ_p the pulse width of 20 ns. The material was specified as Al, with isotropic thermal properties: thermal conductivity, $k_{xx} = k_{zz} = 201$ Wm^{-1}K^{-1}, specific heat capacity, $C_p = 900$ J/kg^{-1}K^{-1}, and thermal expansion coefficient, $\alpha = 2.34 \times 10^{-5}$ K^{-1}; and isotropic elastic properties: Young's modulus, $E = 69$ GPa, density, $\rho = 2720$ kg/m^3 and Poisson's ratio, $v = 0.33$, drawn from the Comsol library.

The surface heat flux can be simplified to a pure elastodynamic surface force dipole model shown in Fig. 1b when the effect of thermal diffusion is negligible, which provides a validation case for the FE procedure as it can be compared to analytical solutions. A horizontal point load with unit force (1 N) was applied to the element node nearest to the centre (at a distance of 9×10^{-6} m), to get as close as possible to representing a point force dipole, as shown in the close-up view of Fig. 1b. A broadband excitation signal was used as the temporal profile of the applied load, given by

$$F_{in,gen} = \frac{1}{2}[1 + \text{erf}(\frac{t - 2\tau_p}{\tau_p})] \tag{2}$$

where t is time, and $\tau_p = 20$ ns is the pulse width. Eq. (2) is the integral of Eq. (1) with respect to t, as the displacement generated is proportional to the rate of change of volumetric strain [2].

2.1.2. Buried source in heterogeneous anisotropic media

The LU source was represented by a buried heat source, as the thermal expansion takes place on the surface of the fibre under a resin layer, where the laser energy is absorbed. A buried heat source with Gaussian distribution in the x-direction and in time (Eq. (1)) was simulated, and the simulation domain is shown in Fig. 1c.
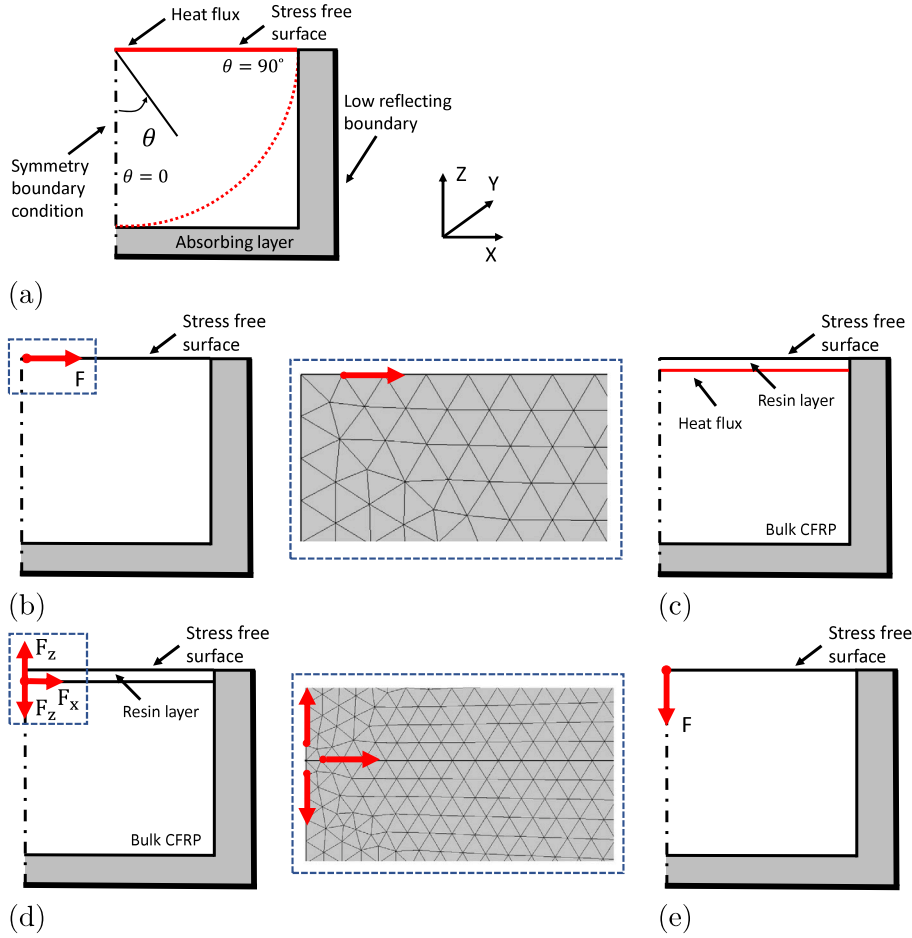
Fig. 1. Schematic drawings of different LU source models. (a) Surface heat flux for Al, (b) surface force dipole for Al, (c) buried Gaussian heat flux for CFRP, (d) buried quadrupole for CFRP and (e) normal point load for the receiver sensitivity in CFRP. The positions of the applied load for the force dipole and buried quadrupole are shown in the zoomed-in figures in (b) and (d).

The CFRP material was modelled as an anisotropic bulk material instead of individual layers, as the interest of the current paper is in the direction of the ultrasound propagation, rather than detailed waveforms resulting from ply reflections. The fibres in each ply are orientated at some angle in the x-y plane, while the through-thickness is in the z-direction. Anisotropic thermal conductivity was modelled for the bulk CFRP material, where $k_{xx} = 7$ $Wm^{-1}K^{-1}$ (parallel to fibre) and $k_{zz} = 0.8$ $Wm^{-1}K^{-1}$ (perpendicular to fibre) [14]. Other thermal properties are, specific heat capacity, $C_p = 710$ J/(kg K) [15], and thermal expansion coefficient, $\alpha = 1.85 \times 10^{-6}$ K^{-1} [16]. The density is $\rho = 1570$ kg/m^3. The elastic constants were estimated using the Backus method based on the ply layup [17], using textbook elastic constants for carbon fibres, where $c_{11} = c_{22} = 12.8$ GPa, $c_{13} = 8$ GPa, $c_{33} = 125$ GPa, $c_{44} = c_{55} = 5.5$ GPa, $c_{66} = 3.75$ GPa, $c_{12} = c_{11} - 2c_{66}$ [18,19]. For the resin layer, isotropic thermal properties were used: $k_{xx} = k_{zz} = 0.2$ $Wm^{-1}K^{-1}$ [20], $C_p = 1884$ J/(kg K) [15], and $\alpha = 65 \times 10^{-6}$ K^{-1}. The elastic properties were also specified to be isotropic, with $E = 5$ GPa, $\rho = 1140$ kg/m^3, and $\upsilon = 0.389$. The source depth was determined by measuring the resin layer thickness.

A buried quadrupole was simulated to emulate the multi-physics model to pure elastodynamics, as shown in Fig. 1d. The force pairs in opposite directions have a separation of 9×10^{-6} m, as shown in the close-up view in Fig. 1d. The amplitude of the force pair in the x-direction, F_x, is set to be greater than that of the force pair in the z-direction, F_z, to account for the anisotropic thermal properties in the multi-physics model. The excitation signal is the same broadband signal used for the force dipole, given by Eq. (2).

2.1.3. Receiver sensitivity

The knowledge of the receiver sensitivity to the L and S waves is required for comparison to experimental results. By reciprocity, the receiver sensitivity is the same as applying a normal point load on the free surface, as the reception laser detects out-of-plane displacements. For the Al case, it is solved in [21].

The receiver sensitivity of LU in CFRP is unknown due to the lack of closed form analytical solution. It was obtained by running a computational model applying a normal point load on the free surface shown in Fig. 1e. A 2-cycle toneburst defined by

$$F_{in,det} = e^{-\left(\frac{t - \frac{2}{f}}{\frac{1}{2f}}\right)^2} \sin(2\pi f t) \qquad (3)$$

was used as the excitation signal.

2.2. Head wave suppression

For a FE model with a finite-sized domain, the measured shear wave displacement contains contributions from both the directly generated shear wave of interest and a head wave. The latter decays more rapidly than the shear wave at any given angle. In contrast, the analytical solution predicts the displacement in the far field, where the head wave is negligible. Therefore, a method to subtract the head wave in FE is described, enabling a better approximation of the far field directivity from a modest-sized modelling domain (0.01 m). This model takes ~ 5 hours to run. In contrast, the estimated size of domain required for the head wave to have decayed to 5% of the amplitude of the direct

shear wave is 0.12 m, i.e. 12 times larger. The associated increase in degrees of freedom for a 2D model is 12^2 and the model will need to run for 12 times the wave propagation time leading to $\sim 12^3$ greater computational cost, which extrapolating from the current modelling time of 5 h would be almost 1 year.

The characteristics of the head wave are mentioned in the literature [22,23]. It can be seen as generated by a source moving at the L wave velocity on the free surface. Therefore, a wave field dominated by head wave, $\mathbf{u}_h(x,z,t)$, was artificially simulated by taking the surface displacement resulting from a LU source model, $\mathbf{u}_f(x,z,t)$, as the boundary condition, and excluding the initial displacement from which all other wave modes were generated. A smooth ramp function was applied to the free surface displacement in the time domain, given by

$$\mathbf{u}(x,t) = \mathbf{u}_0(x,t)\ S(t),$$

where $u_0(x,t)$ are surface displacements measured from the model containing full wavefields and $u(x,t)$ are the surface displacements imposed on the head wave dominated model. It acts as a time window filter to suppress the initial displacement, without introducing extra bulk waves by keeping the first derivatives of the displacements continuous. The smooth ramp function, $S(t)$, is given by

$$S(t) = \begin{cases} 0 & \frac{t}{\beta\tau} \leq 0 \\ 3(\frac{t}{\beta\tau})^2 - 2(\frac{t}{\beta\tau})^3 & 0 \leq \frac{t}{\beta\tau} \leq 1, \\ 1 & 1 \leq \frac{t}{\beta\tau} \end{cases} \tag{4}$$

where the length of the smooth ramp is controlled by the adjustable parameter β which defines its length as a multiple of the duration of the frequency-filtered wave packet, τ. The directivity extraction was performed on the resulting wavefield after subtraction, $\mathbf{u}_s(x,z,t) = \mathbf{u}_f(x,z,t) - \mathbf{u}_h(x,z,t)$.

2.3. Mode and directivity extraction

The displacement of a particular wave mode generated by a source is dependent on the propagation distance, r, and the observation angle, θ. For the 2D case of a cylindrical wavefront, the far-field displacement can be written as

$$u(r,\theta) = D(\theta)\frac{e^{ikr-\omega t}}{\sqrt{r}}, \tag{5}$$

where $D(\theta)$ is the directivity, defined as the amplitude of the wave at unit distance away from the source. From the FE model, the directivity is extracted at a constant distance away from the source where different wave modes can be well separated in time, as indicated by the red arc in Fig. 1a .

The general procedure for extracting the directivity of a particular wave mode from u (x-component) and v (y-component of the displacement) from FE is

1. apply a square time window to u and v, so that each time-windowed displacement signal contains only one wave mode;
2. take the dot product of time-windowed u and v with polarisation vector of corresponding wave modes;
3. apply a frequency filter if a broadband excitation signal was used;
4. obtain the peak amplitude of the wave packet.

The process to compute the polarisation vectors for anisotropic materials are described in detail in [24].

2.4. Validation against analytical result for Al

2.4.1. Analytical solution for Al

The analytical solution for the far-field directivity of a surface force dipole can be obtained by superposing the displacement generated by point forces, for benchmarking the FE model. The exact displacement generated by a single horizontal unit point force (in the x-direction) on the free surface of an isotropic elastic half space in 2D is given by [21],

$$u_L^x(R,\theta) \sim \frac{e^{i(3/4\pi-R)}}{c_{44}}\sqrt{\frac{2}{\pi R}}\frac{\sin 2\theta\sqrt{\mu^2 - \sin^2\theta}}{F_0(\sin\theta)}, \tag{6}$$

and

$$u_S^x(R,\theta) \sim \frac{e^{i(3/4\pi-\mu R)}}{c_{44}}\sqrt{\frac{2\mu^7}{\pi R}}\frac{\cos\theta\cos 2\theta}{F_0(\mu\sin\theta)}, \tag{7}$$

where the longitudinal (L) wave directivity u_L^x and the shear (S) wave directivity u_S^x are functions of R, defined as the product of the distance from the source and the longitudinal wavenumber, $R = k_L r$, and $\mu = \sqrt{c_{11}/c_{44}} = k_S/k_L$ is the ratio of the shear wave number to the longitudinal wavenumber, which relates the two elastic constants, c_{11} and c_{44}. $F_0(\zeta)$ is defined by $F_0(\zeta) = (2\zeta^2 - \mu^2)^2 - 4\zeta^2\sqrt{\zeta^2 - 1}\sqrt{\zeta^2 - \mu^2}$.

A surface force dipole consists of two such horizontal point forces in opposite directions. The dipole strength is product of the magnitude of the force and the separation between the forces. The displacements generated by a dipole of unit strength are related to Eqs. (6)–(7) by

$$u_L^{dip}(R,\theta) \sim i\sin\theta\ u_L^x(R,\theta), \tag{8}$$

and

$$u_S^{dip}(R,\theta) \sim i\mu\sin\theta\ u_S^x(R,\theta). \tag{9}$$

Detailed derivations are given in A.

2.4.2. Benchmarking of FE directivity for Al

Four wave modes generated by the force dipole (Fig. 1b) that propagate in the simulation domain are shown by the displacement magnitude contour in Fig. 2a: the Rayleigh wave, the longitudinal (L) wave, the shear (S) wave. A head wave dominated displacement field shown in Fig. 2b was generated as specified in Section 2.2, with the parameter of the smooth ramp optimised to be $\beta = 1$, which is 6.5×10^{-7} s for waves filtered with $f_c = 5$ MHz at 100% bandwidth. The displacement field after subtraction of Fig. 2b from Fig. 2a shows only the L and S wave generated from the source (Fig. 2c).

The peak displacement amplitude of the L and S waves are extracted, and compared with analytical solution (Eqs. (8)–(9)) for a surface force dipole of unit strength, as shown in Fig. 3. The directivity for the L wave shows good agreement, and the amplitude from FE is lower than the analytical solution due to numerical diffusion. The S wave directivity from FE agree better with analytical solution after head wave subtraction, which effectively removed the extra amplitude in the range 35°–50° due to the head wave and the Rayleigh wave near 90°. The subtraction method hence provides a way to obtain far field directivity from small simulation domains. The loss in the peak amplitude of the FE model at 30° (the critical angle) is attributed to the mesh element size.

3. Experimental measurement procedure

3.1. Set up

Various attempts have been made to measure the directivity of LU in previous studies [10,25–27], using different shapes of samples and different ultrasound detection methods. In the current paper, rectangular samples were used instead of semi-cylindrical samples, as flat surfaces were easier to take measurements. The generation and detection of ultrasound were performed by lasers in a through-transmission
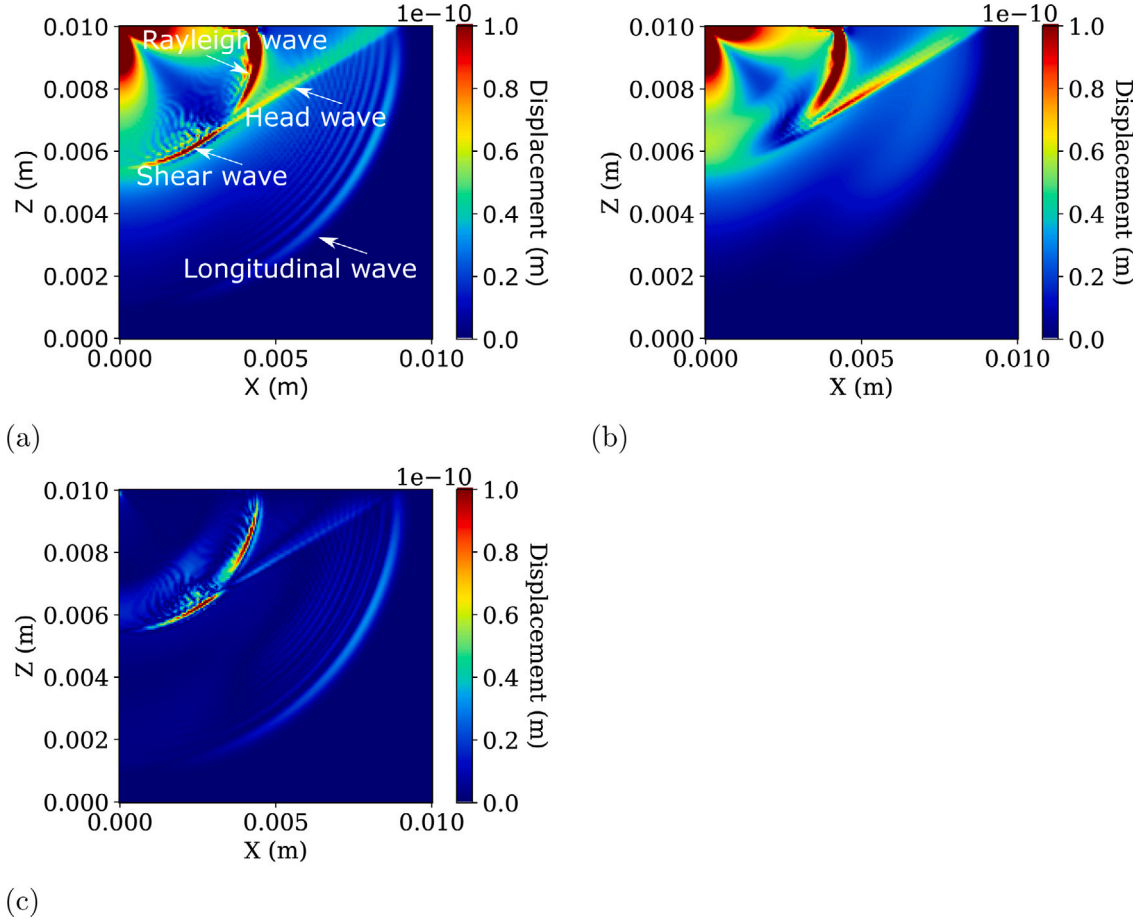
Fig. 2. Displacement magnitude of (a) the force dipole model described in Fig. 1b, $u_f(x, z, t)$, (b) the head wave dominated model, $u_h(x, z, t)$, and (c) the subtracted wavefield, $u_s(x, z, t)$, when $t = 1.55$ μs.
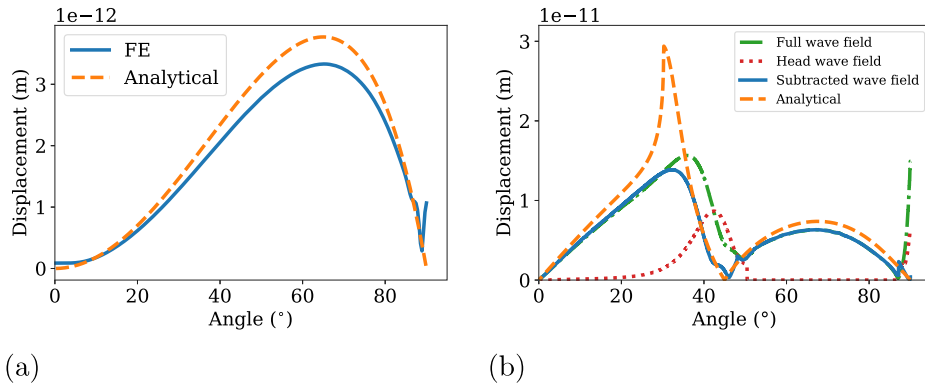

Fig. 3. Absolute displacement of (a) the L wave and (b) the S wave with the head wave subtraction process extracted from the FE force dipole model, compared to analytical solution.

configuration, as shown in Fig. 4a. The generation laser was focused by a cylindrical lens to a line source with a width of 0.2 mm and a length of 6 mm on the sample, so that the directivity in the plane of interest is enhanced and the measurements taken fit in 2D models. The set up of the two experiments are summarised in Table 1.

The detection laser was scanned relative to the generation laser. For the Al case, the generation laser was kept static, and the detection laser was scanned in the x-direction, as shown in Fig. 4b. The rougher and less reflective surface of CFRP compared to Al means that it is harder to make reliable measurements of surface displacement if the

detection laser is scanned. For this reason, the detection laser position was adjusted until a high amplitude, low-noise response was found and then kept at that position while the generation laser was scanned on the other side of the sample. A step size of 1 mm gave coarsest angle increments of 0.22° for Al and 0.51° for CFRP. A scan range of 75 mm in the x-direction on the Al sample gave the directivity measurement in the range 0–70°, with some data points on the other side of the symmetry line for determining the 0 position. For CFRP, the scan range in the x-direction was limited to 30 mm with 60° the maximum angle
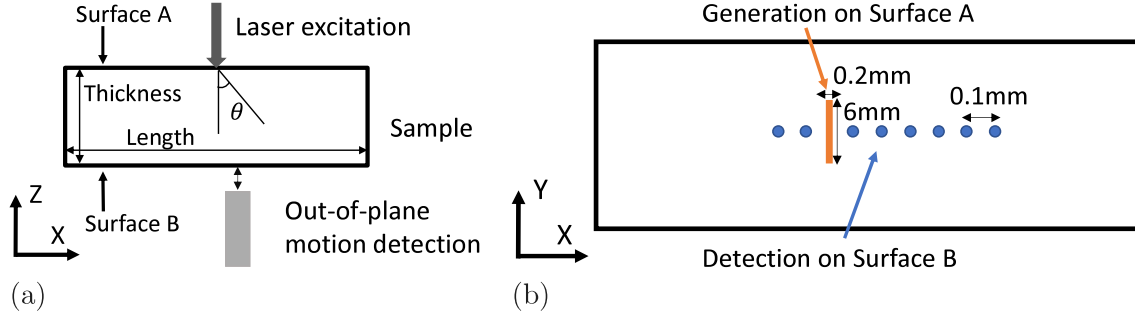
Fig. 4. (a) Schematic drawing of the experimental setup for measuring directivities. (b) Representations of the arrangement and orientation of the generation and detection laser on sample surfaces.

Table 1
Laser and sample specification for the experiments. The measurement on Al was taken at University of Strathclyde, and the measurement on CFRP was taken at University of Bristol.

	Al	CFRP
Generation laser	Nd:YAG	Nd:YAG
Energy per pulse (mJ)	0.75	2
Pulse width (ns)	7	15
Detection laser	Sound & Bright	Sagnac interferometer [28]
	Quartet interferometer	
Sample thickness (mm)	25.8	11.2
Scan range (°)	0–70	0–60

measured, as beyond this angle the signal became indistinguishable from noise due to attenuation.

3.2. Data processing and fitting

As the experimental measurements were taken at different distances away from the source, the data needed to be corrected for beam spreading. This was achieved by multiplying the signal amplitude by $\sqrt{d}$ (d is the distance from the measuring point to the source). Even though the generation laser excites over a line that is 6 mm long, the 2D correction based on an infinitely-long line source is still appropriate as all the measuring points are within the Rayleigh distance [29].

Due to the different scales of the excitation sources and the presence of noise in experiments, a systematic way of scaling the FE data to the experimental data was used. The measured ultrasonic signal was assumed to contain additive Gaussian noise with RMS amplitude, σ. Therefore, the signal envelope obtained after frequency filtering and Hilbert transform can be described by a Rician distribution with parameters, ν and σ, where ν is the noise-free amplitude. For an individual measurement at a particular angle, x_i, the probability density function (PDF) is given by

$$p_i = f(x_i | \nu, \sigma),$$ (10)

where $\nu = \alpha z$, α is the scaling factor from FE to experiment, z is the value from FE at that angle, and σ is the noise level. The probabilities of individual measurement are assumed to be independent of each other. For a given FE and experiment comparison, the unknown α, and σ are adjusted until the overall likelihood function, L_{max}, is maximised, which is given by

$$L_{max} = \sum_{i=1}^{n} \log(p_i),$$ (11)

where n is the number of experimental data points. $\overline{L}_{max} = L_{max}/n$ is provides a quantitative way of comparing the fit for different FE models.

4. Results and discussion

4.1. Effect of source type in Al

The experimentally measured directivity was extracted from the raw A-scans of the Al sample (Fig. 5a) for comparison of the force dipole and surface heat flux model. The absolute displacements shown in Fig. 5a were calculated according to the calibration of the detection laser (Quartet, Sound & Bright, Inglewood, CA, USA), 100 mV/nm, and then frequency-filtered with a Gaussian filter, f_c = 5 MHz, and 100% bandwidth measured at −40 dB, and scaled for beam spreading (Fig. 5b). The amplitude of each mode was obtained by extracting the peak amplitude of the signal envelop within a short time window around the expected arrival time, as indicated, for example, by the white lines bracketing the L-wave signal in Fig. 5b.

The surface heat flux model was simulated and the head wave subtraction process was applied to obtain a better approximation of the far field directivity for the S wave. The directivities of the force dipole and surface heat flux model for Al, multiplied by the receiver sensitivity, were fitted to the experimental data using the maximum likelihood for Rician distribution, as shown in Fig. 6. The maximum likelihood averaged over the number of data points, $\overline{L}_{max}$, was used as an indicator of the goodness of the fit, which was obtained by finding a common scaling factor from FE to experimental data, α, and a common noise level, σ across all wave modes and all measured angles for each model. $\overline{L}_{max} = 0.0892$ with $\alpha = 3.22$ and $\sigma = 3.26 \times 10^{-4}$ for the force dipole model, and $\overline{L}_{max} = 0.0867$ with $\alpha = 1.73 \times 10^5$ and $\sigma = 2.90 \times 10^{-4}$ for the heat flux model. The $\overline{L}_{max}$ for both models on both wave modes show sufficiently similar figures to justify the use of a dipole model in Al as it is close enough to the heat flux model.

The deviation of modelled S wave directivity from experimental data is mainly attributed to the presence of head wave in experimental data, as the main directivity lobe is seen to be wider than the modelled results. The directivity extracted from the heat flux model has higher amplitude at smaller angles, since this lies directly below the source and is subject to the downward thermal expansion, effectively creating an offset. For the L wave, this extra amplitude coincides with the noise floor. Although visually the heat flux model directivity is a better fit to the experimental data than the dipole model directivity (Fig. 6a), the $\overline{L}_{max}$ figure does not show significant difference, because the noise is always positive. The heat flux model can be related to the force dipole by calculating the dipole strength from the stresses induced on the free surface. This simplifies the multi-physics model to the elastodynamic model, by converting the thermal stress to elastodynamic stress and ignoring thermal diffusion.

The relative amplitude of the S wave and L wave signal are also shown in Fig. 6, with the S wave amplitude being ∼ 10 times larger than the L wave, in line with various literature [3,30]. Therefore the S wave is more commonly used for NDE inspection in thermoelastic regime than the L wave. However, the directivity needs to be taken
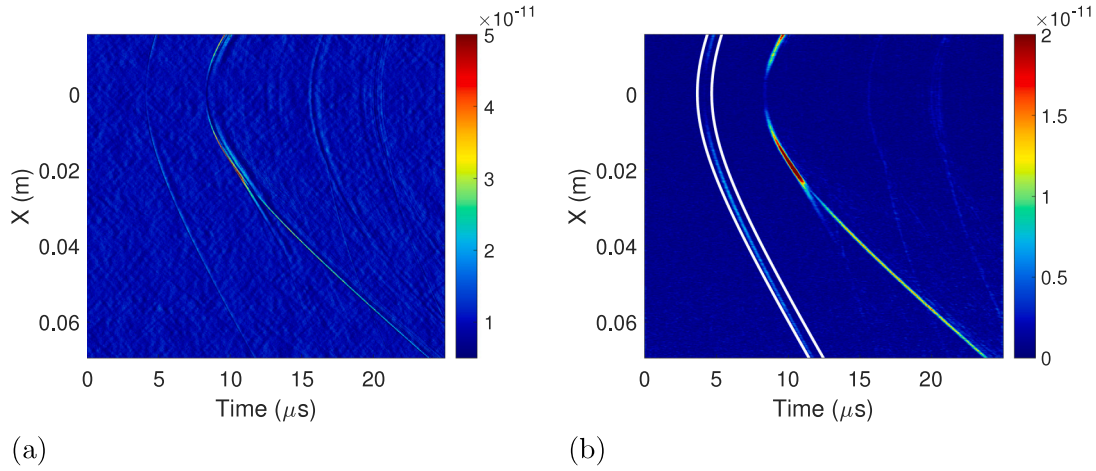
Fig. 5. (a) Raw A-scans, and (b) A-scans compensated for beam spreading based on propagation distance for the Al sample, filtered at f_c = 5 MHz, 100% bandwidth. White lines show examples of time windows for the extraction of directivities.
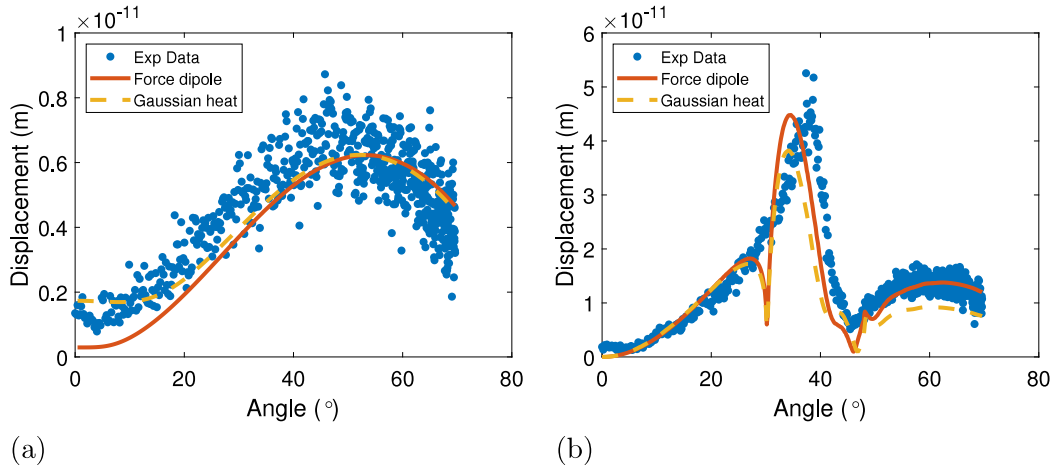

Fig. 6. Directivity extracted from the force dipole model and Gaussian heat flux model in Al multiplied by the receiver sensitivity.

into account when designing inspection. There is no signal directly below the source, and the signal maximum occurs at the critical angle (30°). However, this has varying amplitude based on the propagation distance, due to the head wave.

4.2. Effect of source type in CFRP

The experimentally measured directivity was extracted from the raw A-scans of the CFRP sample (Fig. 7a) for the comparison of the buried Gaussian distributed heat source and buried quadrupole model. Fig. 7 shows arbitrary displacement magnitude, as the Sagnac interferometer is uncalibrated. The qL wave and the qS wave are found to have different frequency content because the qS wave is more rapidly attenuated in the CFRP material. The main mechanism is attributed to the qS wave has shorter wavelength relative to ply thickness ratio causing more reflection from plies, and the shear motion in qS wave is more affected by viscoelastic damping than the compression and expansion in qL wave. For this reason, the CFRP A-scans were frequency-filtered by a Gaussian filter at f_c = 2.5 MHz and 100% bandwidth at −40 dB for the directivity of the qL wave, and at f_c = 1.5 MHz and 100% bandwidth at −40 dB for the directivity of the qS wave. The CFRP sample appears as homogeneous to both wave modes filtered at these low frequencies, and no ply reflections are seen, because the wavelength is much longer than the ply thickness (0.25 mm). Fig. 7b shows an example of a square time window (indicated by the white lines) applied to extract the peak amplitude for the qL wave.

The relevant properties of the CFRP sample were determined. The laser source was estimated to be 0.1 mm below the surface, as shown by the close up cross-sectional view in Fig. 8a. Fibre running in the plane of the cross-section image is denoted as 0° in the markup in Fig. 8b, and fibre running normal to the cross-section image as 90°, and similarly for ±45°. Therefore, based on the stacking sequence indicated in the image, the elastic property of the sample lies between that of a cross-ply ([0,90]) and a quasi-isotropic layup ([0, ± 45,90]) as a first approximation. The Backus method calculates the range of the elastic constants to be c_{11} = [68.9, 56.4] GPa, c_{12} = [8.04, 20.5] GPa, c_{66} = [5.50, 18.0] GPa, while c_{13} = 7.25 GPa, c_{33} = 12.8 GPa, c_{44} = 4.46 GPa are the same for both layups. The Backus method for estimating the elastic constants requires the wavelength to be much longer than the thickness of the medium being averaged over [17]. c_{11}, c_{12}, and c_{66} were then incrementally adjusted to find a good fit to the qL wave velocity measured in the experiment, as shown in Fig. 8c. The final homogenised stiffness matrix used for the FE model is given by

$$C = \begin{pmatrix} 63.1 & 8.04 & 7.25 & 0 & 0 & 0 \\ 8.04 & 63.1 & 7.25 & 0 & 0 & 0 \\ 7.25 & 7.25 & 12.8 & 0 & 0 & 0 \\ 0 & 0 & 0 & 4.46 & 0 & 0 \\ 0 & 0 & 0 & 0 & 4.46 & 0 \\ 0 & 0 & 0 & 0 & 0 & 5.50 \end{pmatrix} \text{GPa.} \quad (12)$$

The head wave subtraction process of the CFRP case is shown in Fig. 9, using the buried Gaussian distributed heat source model as an
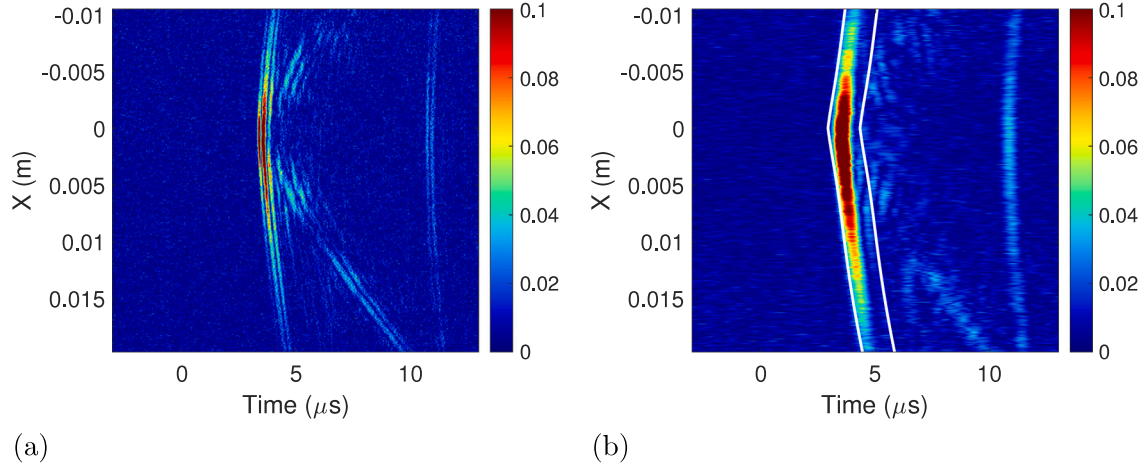
Fig. 7. (a) Raw A-scans, and (b) A-scans compensated for beam spreading based on propagation distance for the CFRP sample, filtered at f_c = 2.5 MHz, 100% bandwidth. White lines show examples of time windows for the extraction of directivities.
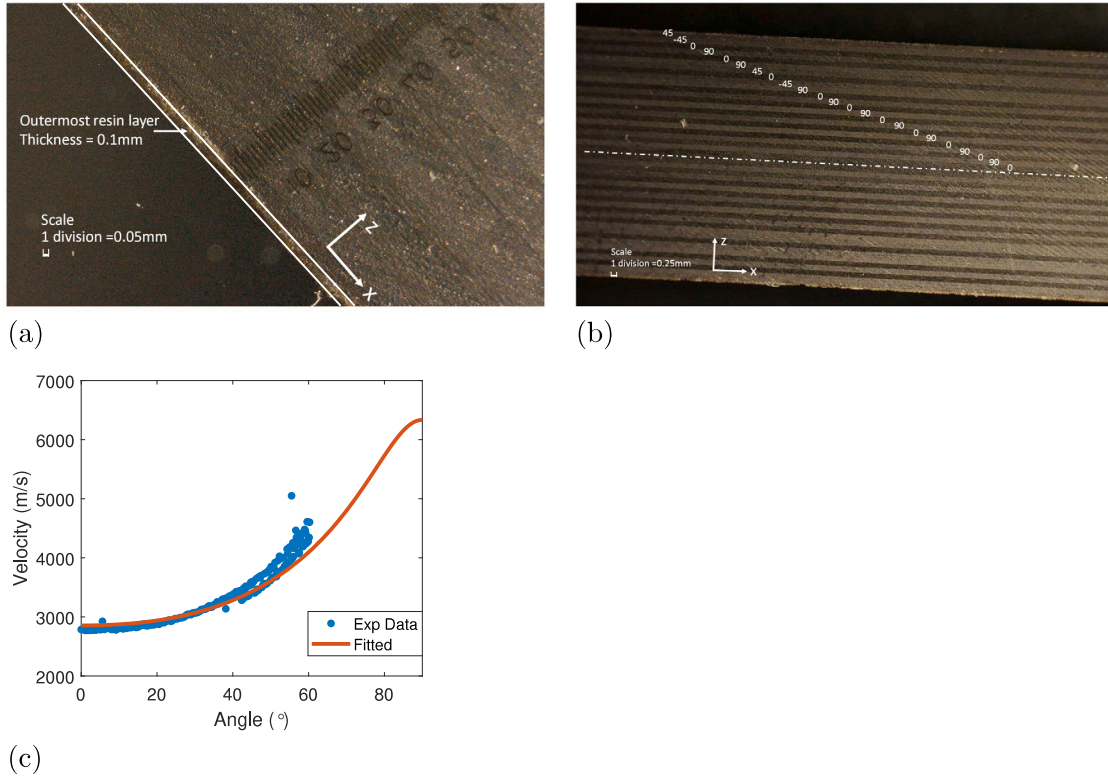

Fig. 8. (a) Measurement of the resin layer thickness under a microscope. (b) Cross-section of the CFRP sample under a microscope, labelled with ply orientation. (c) qL wave velocity computed from approximated elastic constants using the Backus method compared with those calculated from arrival time of the A-scans in Fig. 7a.

example. For buried sources, the out-of-plane displacements on the symmetry boundary as well as the surface displacements need to be multiplied by the smooth ramp function and enforced in the head wave model (Fig. 9b), in order to match the equivalent wavefield of the original model (Fig. 9a). From the subtracted wavefield in Fig. 9c, the qS wave shows cuspoidal wavefronts. The directivity extracted from the qS wave excludes the amplitude on the cusp.

The relative amplitudes of the force pairs, F_x and F_z, of the buried quadrupoles were adjusted until the directivities show a close match to the multi-physics model, which is set to be $F_x = 5F_z$. The normalised directivities of the qL wave and the qS wave of the two CFRP models and the receiver sensitivity are shown in Fig. 10.

The directivity of buried Gaussian distributed heat sources and buried quadrupole are compared to experimental data of CFRP in Fig. 11. The amplitudes have arbitrary units due to the uncalibrated detection laser, but the relative amplitudes between the two wave modes are preserved, which can be seen from Fig. 11. $\overline{L}_{max} = 0.0887$, with $\alpha = 5.16 \times 10^{17}$ and $\sigma = 0.0112$ for the qL wave of the buried Gaussian distributed heat sources, and $\overline{L}_{max} = 0.0859$, with $\alpha = 5.98 \times 10^{12}$ and $\sigma = 0.0122$ for the qL wave of the buried quadrupole. $\overline{L}_{max} = 0.0853$, with $\alpha = 9.50 \times 10^{16}$ and $\sigma = 0.0187$ for the qS wave of the buried Gaussian distributed heat sources, and $\overline{L}_{max} = 0.0851$, with $\alpha = 1.00 \times 10^{12}$ and $\sigma = 0.0194$ for the qS wave of the buried quadrupole. $\overline{L}_{max}$ is obtained separately for the qL and qS wave as their directivities
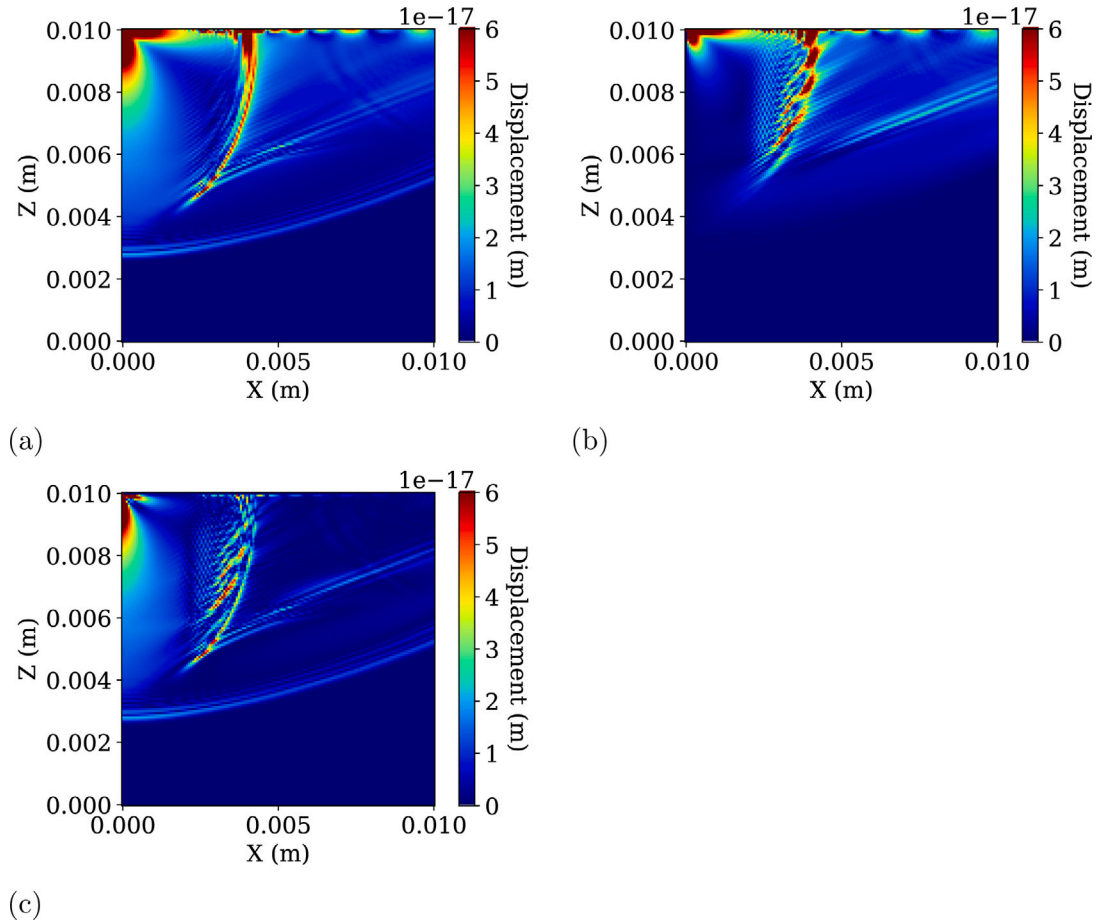
Fig. 9. Displacement magnitude of (a) the buried Gaussian distributed heat source model described in Fig. 1c, $\mathbf{u}_f(x, z, t)$, (b) the head wave dominated model, $\mathbf{u}_h(x, z, t)$, and (c) the subtracted wavefield, $\mathbf{u}_s(x, z, t)$, when $t = 2.7$ μs.
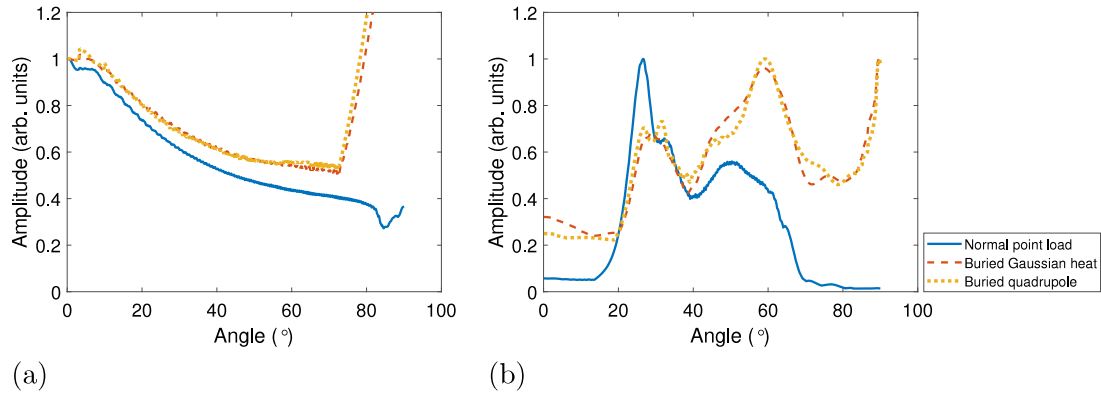

Fig. 10. Normalised directivities of (a) the qL wave and (b) the qS wave from all CFRP models.

were extracted at different frequencies. The frequency response of the experimental instrumentation and the frequency-dependent attenuation do not guarantee a common α to be found for both wave modes. The directivity patterns measured show some extent of asymmetry as the generation laser was slightly out-of-focus for some parts of the scan, which is caused by the generation laser beam not being perpendicular to the scanning path due to spatial restrictions on the arrangement of equipment. Larger discrepancy between the FE and experimental directivity is seen between 0–20° for the qS wave due to the noise floor of the experimental measurement. The noise level in the CFRP case is much greater than the Al case due to lower surface reflectivity of the CFRP sample. The elastodynamic model is seen as a good

representation of the LU source, and provides greater simplicity than the multi-physics model. The values of $\overline{L}_{max}$ for the CFRP case are within 5% difference from the $\overline{L}_{max}$ for the Al case, suggesting that the FE modelling strategy can be adequately used for complex materials.

For the CFRP sample, the qL wave shows a maximum amplitude directly below the source, as the resin layer above the centre of expansion supports normal stresses. This makes it more advantageous for NDE inspection than the qS wave. The qS wave amplitude is only $\sim 1/3$ of the qL wave amplitude due to severe attenuation, and the cuspidal wavefronts also raise more complex issues for signal processing. The modelled directivity can be used directly to weight the imaging for suppressing noise, or to feed to forward models of LU inspections.
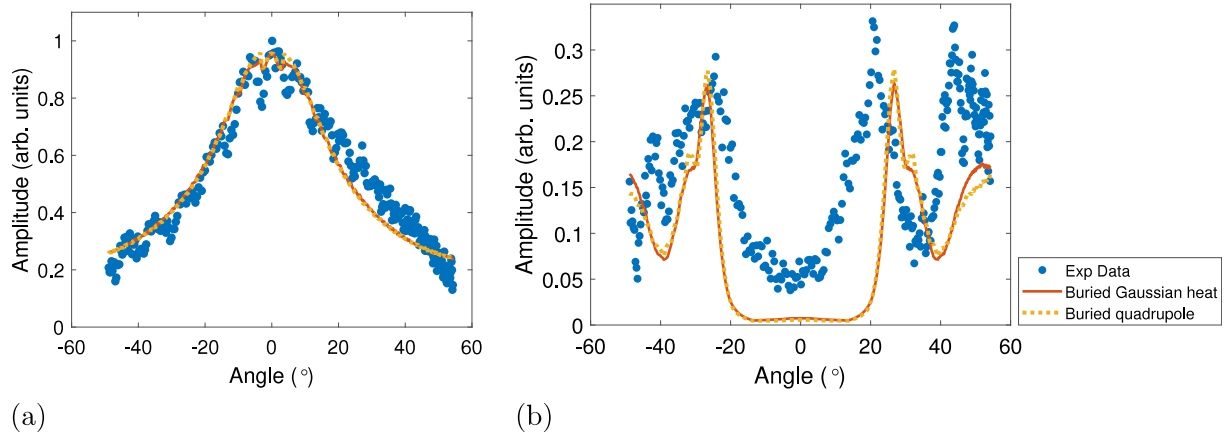
Fig. 11. Directivity extracted from the buried quadrupole model and buried Gaussian heat flux model in CFRP multiplied by the receiver sensitivity, compared to experimental measurements for (a) the qL wave, and (b) the qS wave.

Although FE provides maximum flexibility and the ability to include multi-physics effect, the strategy to extract modal directivity from FE proposed here is still not without limitations. This motivates future work to extend analytical methods to at least cover more complex elastodynamics cases.

5. Conclusion

An FE modelling methodology for LU source on different materials to obtain the directivity of the ultrasound is presented and demonstrated through two practical examples. The general steps of the method include the set up of the modelling domain, the head wave subtraction process to obtain an approximation of the far-field directivity of the shear waves from a small simulation domain, and the mode and directivity extraction from the FE output. The outcome of the modelling can be incorporated into forward models for simulating LU inspection datasets and to assist the design of inspections, particularly in scenarios when the analytical solutions are not available, for example, in anisotropic layered media.

The isotropic Al case provides a benchmark analytical solution for the elastodynamic model of a surface force dipole. The modelling method is applied to a multi-physics model of a surface Gaussian distributed heat flux. The heterogeneous anisotropic CFRP case shows the modelling method can be applied to more complex scenario, where the multi-physics model of a buried point heat source and a buried Gaussian distributed heat source take into account details such as anisotropic thermal properties. A buried quadrupole model is simulated to show that the similar effect can be obtained from a pure elastodynamic model. The comparison to experimental measurements show that the elastodynamic model for both cases are sufficient to represent the LU source.

CRediT authorship contribution statement

Xin L. Tu: Writing – original draft, Methodology, Formal analysis, Conceptualization. **Jie Zhang:** Writing – review & editing, Supervision, Methodology, Conceptualization. **Alberto M. Gambaruto:** Writing – review & editing, Supervision, Methodology, Conceptualization. **Paul D. Wilcox:** Writing – review & editing, Supervision, Methodology, Funding acquisition, Conceptualization.

Declaration of competing interest

The authors declare that they have no known competing financial interests or personal relationships that could have appeared to influence the work reported in this paper.

Data availability

Data will be made available on request.

Appendix A. Derivation of force dipole directivity

The displacement of the L wave generated by a force in the x-direction Eq. (6) can be summarised by

$$u_L^x(R, \theta) = F \frac{1}{\sqrt{R}} D(\theta) e^{iR},$$

where F is the amplitude of the applied force. A force dipole is formed by two such forces in opposite directions. Let the separation between the forces be δ/k_L, and the amplitude of each force be F/δ, the displacement at r with the midpoint between the forces as the origin is given by

$$u_L^{dip}(R, \theta) = u_L^x(R_1, \theta_1) - u_L^x(R_2, \theta_2),$$

where R_1 and R_2 are related to the distances from each force to the observation point by k_L. Using paraxial approximation for far field solutions,

$$R_1 \simeq R - \frac{\delta}{2} \sin \theta,$$

and

$$R_2 \simeq R + \frac{\delta}{2} \sin \theta.$$

The difference between R, R_1, and R_2 are negligible for beam spreading, i.e. $\sqrt{R} \cong \sqrt{R_1} \cong \sqrt{R_2}$, but needs to be accounted for in the exponentials. This gives

$$
\begin{aligned}
u_L^{dip}(R, \theta) &= \frac{F}{\delta} \frac{1}{\sqrt{R}} D(\theta)[e^{i(R + \frac{\delta}{2} \sin \theta)} - e^{i(R - \frac{\delta}{2} \sin \theta)}] \\
&= \frac{F}{\delta} \frac{1}{\sqrt{R}} D(\theta) e^{iR}[e^{i \frac{\delta}{2} \sin \theta} - e^{i \frac{\delta}{2} \sin \theta}] \\
&= \frac{F}{\delta} \frac{1}{\sqrt{R}} D(\theta) e^{iR} 2i \sin(\frac{\delta}{2} \sin \theta).
\end{aligned}
$$

Take the limit $\delta \to 0$, $\sin(\frac{\delta}{2} \sin \theta) \to \frac{\delta}{2} \sin \theta$, so

$$u_L^{dip}(R, \theta) = F \frac{1}{\sqrt{R}} i D(\theta) \sin \theta e^{iR}$$

$$= i \sin \theta u_L^x(R, \theta).$$

For the S wave, define $R_S = k_S/k_L R = \mu R$, therefore,

$$R_{S,1} \simeq \mu R - \frac{\delta}{2} \mu \sin \theta,$$

and

$$R_{S,2} \simeq \mu R + \frac{\delta}{2} \mu \sin \theta.$$

Going through the same derivation gives

$$u_S^{dip}(R, \theta) = i \mu \sin \theta u_S^x(R, \theta).$$

References

[1] J.-P. Monchalin, Laser-ultrasonics: Principles and industrial applications, in: Ultrasonic and Advanced Methods for Nondestructive Testing and Material Characterization, World Scientific, 2007, pp. 79–115.

[2] C.B. Scruby, L.E. Drain, Laser Ultrasonics: Techniques and Applications, Routledge, 2019.

[3] T. Stratoudaki, M. Clark, P.D. Wilcox, Laser induced ultrasonic phased array using full matrix capture data acquisition and total focusing method, Opt. Express 24 (19) (2016) 21921–21938.

[4] T. Stratoudaki, M. Clark, P.D. Wilcox, Full matrix capture and the total focusing imaging algorithm using laser induced ultrasonic phased arrays, in: AIP Conference Proceedings, vol. 1806, (no. 1) AIP Publishing LLC, 2017, 020022.

[5] J.-P. Monchalin, Laser-ultrasonics: From the laboratory to industry, in: AIP Conference Proceedings, vol. 700, (no. 1) American Institute of Physics, 2004, pp. 3–31.

[6] D. Pieris, T. Stratoudaki, Y. Javadi, P. Lukacs, S. Catchpole-Smith, P.D. Wilcox, A. Clare, M. Clark, Laser induced phased arrays (LIPA) to detect nested features in additively manufactured components, Mater. Des. 187 (2020) 108412.

[7] P. Lukacs, G. Davis, T. Stratoudaki, S. Williams, C.N. MacLeod, A. Gachagan, Remote ultrasonic imaging of a wire arc additive manufactured Ti-6AI-4V component using laser induced phased array, in: 2021 IEEE International Instrumentation and Measurement Technology Conference, I2MTC, IEEE, 2021, pp. 1–6.

[8] M. Umemoto, S.E. Kruger, H. Ohtsuka, Ultrasonic study on the change in elastic properties of cementite with temperature and Mn content using nearly full density polycrystalline bulk samples, Mater. Sci. Eng. A 742 (2019) 162–168.

[9] S. Liang, D. Levesque, N. Legrand, H.S. Zurob, Use of in-situ laser-ultrasonics measurements to develop robust models combining deformation, recovery, recrystallization and grain growth, Materialia 12 (2020) 100812.

[10] J.R. Bernstein, J.B. Spicer, Line source representation for laser-generated ultrasound in aluminum, J. Acoust. Soc. Am. 107 (3) (2000) 1352–1357.

[11] T. Stratoudaki, C. Edwards, S. Dixon, S. Palmer, Laser based ultrasound using different wavelengths for the inspection of composite materials, in: AIP Conference Proceedings, vol. 615, (no. 1) American Institute of Physics, 2002, pp. 316–323.

[12] COMSOL Multiphysics® v. 6.1, 2022, COMSOL AB, Stockholm, Sweden. https://www.comsol.com/.

[13] P. Rajagopal, M. Drozdz, E.A. Skelton, M.J. Lowe, R.V. Craster, On the use of absorbing layers to simulate the propagation of elastic waves in unbounded isotropic media using commercially available finite element packages, Ndt e Int. 51 (2012) 30–40.

[14] N. Saeed, Y. Abdulrahman, S. Amer, M.A. Omar, Experimentally validated defect depth estimation using artificial neural network in pulsed thermography, Infrared Phys. Technol. 98 (2019) 192–200.

[15] H. Xu, J. Hu, Modeling of the material removal and heat affected zone formation in CFRP short pulsed laser processing, Appl. Math. Model. 46 (2017) 354–364.

[16] C. Dong, K. Li, Y. Jiang, D. Arola, D. Zhang, Evaluation of thermal expansion coefficient of carbon fiber reinforced composites using electronic speckle interferometry, Opt. Express 26 (1) (2018) 531–543.

[17] G.E. Backus, Long-wave elastic anisotropy produced by horizontal layering, J. Geophys. Res. 67 (11) (1962) 4427–4440.

[18] Y. Humeida, V.J. Pinfield, R.E. Challis, P.D. Wilcox, C. Li, Simulation of ultrasonic array imaging of composite materials with defects, IEEE Trans. Ultrason. Ferroelectr. Freq. Control 60 (9) (2013) 1935–1948.

[19] H. Cao, S. Guo, Z. He, Y. Xie, T. Zhang, W. Feng, In situ elastic constant determination of unidirectional CFRP composites via backwall reflected multi-mode ultrasonic bulk waves using a linear array probe, Composites B 238 (2022) 109953.

[20] P. Wang, Z. Zhang, B. Hao, S. Wei, Y. Huang, G. Zhang, Investigation on heat transfer and ablation mechanism of CFRP by different laser scanning directions, Composites B (2023) 110827.

[21] G. Miller, H. Pursey, The field and radiation impedance of mechanical radiators on the free surface of a semi-infinite isotropic solid, Proc. R. Soc. London. Ser. A. Math. Phys. Sci. 223 (1155) (1954) 521–541.

[22] J. Achenbach, Wave Propagation in Elastic Solids, Elsevier, 2012.

[23] L.J. Fradkin, A.P. Kiselev, The two-component representation of time-harmonic elastic body waves in the high-and intermediate-frequency regimes, J. Acoust. Soc. Am. 101 (1) (1997) 52–65.

[24] C. Lane, The Development of a 2D Ultrasonic Array Inspection for Single Crystal Turbine Blades, Springer Science & Business Media, 2013.

[25] D. Hutchins, R. Dewhurst, S. Palmer, Directivity patterns of laser-generated ultrasound in aluminum, J. Acoust. Soc. Am. 70 (5) (1981) 1362–1369.

[26] S. Raetz, T. Dehoux, M. Perton, B. Audoin, Acoustic beam steering by light refraction: Illustration with directivity patterns of a tilted volume photoacoustic source, J. Acoust. Soc. Am. 134 (6) (2013) 4381–4392.

[27] M. Dubois, F. Enguehard, L. Bertrand, M. Choquet, J.-P. Monchalin, Numerical and experimental studies of the generation of ultrasound by laser, Le J. de Phys. IV 4 (C7) (1994) C7–689.

[28] I. Pelivanov, T. Buma, J. Xia, C.-W. Wei, M. O'Donnell, NDT of fiber-reinforced composites with a new fiber-optic pump–probe laser-ultrasound system, Photoacoustics 2 (2) (2014) 63–74.

[29] A. Safari, Improved Defect Characterisation Using Ultrasonic Arrays (Ph.D. thesis), University of Bristol, 2020.

[30] L. Rose, Point-source representation for laser-generated ultrasound, J. Acoust. Soc. Am. 75 (3) (1984) 723–732.